Journal of Materials Chemistry A

Monodisperse PdSn/SnOx core/shell nanoparticles with superior electrocatalytic ethanol oxidation performance

Journal:	*Journal of Materials Chemistry A*
Manuscript ID	TA-COM-09-2020-008693
Article Type:	Communication
Date Submitted by the Author:	03-Sep-2020
Complete List of Authors:	Gao, Qiang; Virginia Tech, Department of Chemical Engineering Mou, Tianyou; Virginia Tech, Department of Chemical Engineering Liu, Shikai; National University of Singapore Faculty of Engineering, Materials Science and Engineering Johnson, Grayson; University of Virginia, Chemistry Han, Xue; Virginia Tech, Chemical Engineering Yan, Zihao; Virginia Tech, Department of Chemical Engineering Ji, Mengxia; Virginia Tech, Department of Chemical Engineering He, Qian; National University of Singapore - Kent Ridge Campus, Materials Science and Engineering; National University of Singapore - Kent Ridge Campus, National University of Singapore Zhang, Sen; University of Virginia, Chemistry Xin, Hongliang ; Virginia Tech, Chemical Engineering; Virginia Tech Zhu, Huiyuan; Virginia Tech, Department of Chemical Engineering

COMMUNICATION

Monodisperse PdSn/SnO_x core/shell nanoparticles with superior electrocatalytic ethanol oxidation performance

Received 00th January 20xx,
Accepted 00th January 20xx

DOI: 10.1039/x0xx00000x

www.rsc.org/

Qiang Gao,[a] Tianyou Mou,[a] Shikai Liu,[b] Grayson Johnson,[c] Xue Han,[a] Zihao Yan,[a] Mengxia Ji,[a] Qian He,[b] Sen Zhang,[c] Hongliang Xin,*[a] and Huiyuan Zhu*[a]

Direct ethanol fuel cells are one of the most promising electrochemical energy conversion devices for portable electronics and electric vehicles. Highly efficient and robust electrocatalysts for the ethanol oxidation reaction are therefore desired. In this paper, we report a facile approach for synthesizing monodisperse PdSn/SnO_x core/shell nanoparticles as high-performance catalysts for electrochemical ethanol oxidation reaction (EOR). The mass current density of PdSn/SnO_x reached 3.2 A/mg_{Pd} at 0.85 V vs. RHE in 1 M KOH solution, which is 3.2 times higher than that of the commercial Pd catalyst. More importantly, these PdSn/SnO_x core/shell nanoparticles exhibit enhanced stability compared with the commercial Pd catalyst. Density functional theory calculations suggest that the strong d-p orbital coupling and sp-electron transfer in the PdSn alloy weakens the adsorption of carbonaceous species, e.g., the acetate-evolution intermediate *CH_3CO and the poisoning species *CO, at Pd sites. Consequently, the destabilization of these species facilitates their coupling with *OH, leading to enhanced EOR activity and poison resistance. Meanwhile, we found that amorphous SnO_x layers possess rich Sn-Sn ensembles with stronger adsorption of *OH, providing a shuttling path of hydroxide ions to surface sites.

1. Introduction

As a renewable fuel that can be produced from biomass, ethanol has attracted increasing attention because of the easy-to-store/transport nature, considerably high volumetric energy density (24 MJ/L), low price, and low toxicity.[1-3] Direct ethanol fuel cells (DEFCs) convert chemical energy stored in ethanol to electric energy with much higher efficiency than conventional ethanol-powered engines. DEFCs are particularly attractive to portable and mobile electronic devices due to the lightweight and safe feature while maintaining a high energy density, making them the ideal alternative to batteries in laptops, cell phones, drones, and eventually electric vehicles.[4-7] However, formidable challenges, such as sluggish reaction kinetics, catalyst poisoning, and ethanol crossover, still exist before the large-scale commercialization of DEFCs. Among these challenges, the most critical one is the development of highly active and stable electrocatalysts for the ethanol oxidation reaction (EOR). Current electrocatalysts for EOR suffer from sluggish kinetics and poor stability because of the poisoning of the catalytic active sites by reaction intermediates such as carbonyl (*CO) and acetyl (*CH_3CO)[8]. At present, noble metal Pt-based nanoparticles are the most active electrocatalysts for the EOR. However, their application in large-scale production is limited by their notorious poisoning together with the high cost and scarcity. One solution is to make use of nanostructured Pd and Pd-based alloys as alternatives to Pt-based electrocatalysts due to their higher CO tolerance compared with Pt.[9-12] Alloying Pd with a less expensive secondary transition metal, e.g., Cu,[13] Sn,[1, 14] Pb,[15] and Ni[16], can reduce the usage of Pd while modify its electronic structure to further promote the EOR.[10] Especially, alloying Pd with a post-transition metal, e.g., Pb[15] or Sn[1, 14, 17], weakens the adsorption of poisoning intermediates, and thereby significantly improves the catalytic performance of Pd in the EOR. Nevertheless, the nature of active ensembles of Pd-based catalysts in the EOR remains elusive due to the evolution and restructuring of active sites driven by oxidative potential sweeping.[11] For example, we anticipate that PdSn bimetallic nanocatalysts could phase-segregate to form an oxide or hydroxide layer in alkaline solution during the EOR because of a higher oxophilicity of Sn than Pd, similar to the behavior of bimetallic PdNi,[18] AuMn,[19] AuSn,[20] AuCo,[21] in oxidative annealing treatment. Several studies have shown that the EOR activity of Pd can be significantly enhanced by adding SnO_x, which can accelerate the adsorption of hydroxyl (*OH) on the catalyst surface, promoting the oxidation of ethanol into acetate.[22-24] Consequently, we envision that the co-existence of a SnO_x layer and Sn atoms in the Pd matrix can weaken the adsorption of carbonaceous species, facilitate the coupling with *OH for the formation of acetate and alleviate the surface poisoning. Unfortunately, the atomistic understanding and synthetic control of the metal-metal oxide/hydroxide interface of Pd-based catalysts is still lacking, placing a barrier for optimizing their intrinsic activity and stability during the EOR.

Herein, we design and synthesize monodisperse PdSn/SnO_x core/shell nanoparticles with a size of 4.5 nm ± 0.5 nm. The bimetallic core has a size of 3.5 nm ± 0.5 nm while the tin oxide shell is amorphous with a size of 0.5 nm ± 0.1 nm. The PdSn/SnO_x core/shell nanoparticles were prepared by the co-reduction of palladium(II) chloride ($PdCl_2$) and tin(II) acetate ($Sn(OAc)_2$) with oleylamine (OAm)

[a]Department of Chemical Engineering, Virginia Polytechnic Institute and State University, 635 Prices Fork Rd., Blacksburg, Virginia 24061, USA.
[b]Department of Materials Science and Engineering, National University of Singapore, 9 Engineering Drive 1, 117575, Singapore.
[c]Department of Chemistry, University of Virginia, Charlottesville, Virginia 22904, USA.
E-mail: hxin@vt.edu, and huiyuanz@vt.edu
Electronic Supplementary Information (ESI) available: [details of any supplementary information available should be included here]. See DOI: 10.1039/x0xx00000x

as both the solvent and reducing agent and trioctylphosphine (TOP) as a capping agent (Scheme 1). The carbon-supported PdSn/SnO_x nanoparticles, denoted as C-PdSn/SnO_x, demonstrated a substantially enhanced EOR activity (3.2 A/mg_{Pd} at 0.85 V vs. RHE) as compared with that of commercial C-Pd catalysts (1.0 A/mg_{Pd} at 0.83 V vs. RHE). More importantly, the C-PdSn/SnO_x exhibited much better long-term stability than commercial C-Pd electrocatalyst with only a negligible decrease of peak current density after 1000 potential cycles in 1 M KOH + 1 M ethanol. Density functional theory (DFT) calculations reveal that the formation of surface PdSn alloys reduces the activation barrier of *CH_3CO coupling with *OH, a rate-determining step in Pd-catalyzed EOR.[25] Moreover, the *CO species from *CH_3CO splitting can be significantly destabilized on PdSn, which improves the stability of the catalysts from surface poisoning. Furthermore, the formation of SnO_x layers at the surface provides a reservoir of stable *OH species, which can be transferred to surface sites for coupling with carbonaceous species, benefiting both the activity and stability of the catalyst.

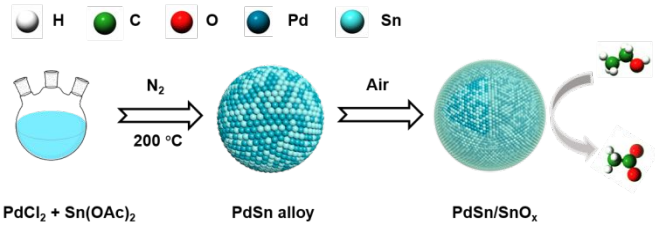

Scheme. 1 Schematic illustration of the synthesis and application of PdSn/SnO_x nanoparticles.

2. Experimental

2.1 Chemicals

Palladium(II) chloride ($PdCl_2$, 99%), tin acetate ($Sn(OAc)_2$, 99%), oleylamine (OAm, 70%), trioctylphosphine (TOP, 90%), potassium hydroxide (KOH), acetic acid, hydrazine, and Nafion (5 wt %) were all purchased from Sigma-Aldrich. Hexane and ethanol were technical grade and used without further purification.

2.2 Synthesis of monodisperse PdSn/SnO_x nanoparticles

In a typical procedure, 0.1 mmol of $PdCl_2$, 0.1 mmol of $Sn(OAc)_2$, 10 mL OAm and 0.5 mL TOP were added into a 50 mL three-necked flask under stirring. The mixture was heated under nitrogen (N_2) atmosphere to 100 °C and kept at this temperature for 30 mins. Then the mixture was heated to 200 °C at a heating rate of 10 °C/min and incubated at this temperature for 30 min, generating a black solution. After cooling down to room temperature, the black precipitate was centrifuged and washed three times with excessive ethanol and redispersed in hexane. PdSn/SnO_x nanoparticles with different Pd/Sn ratios were synthesized using a similar approach by varying the amounts of metal precursors. SnO aggregates were obtained using a similar approach without adding Pd precursor, while 25 nm Pd nanoparticles were obtained at a higher temperature of 300 °C without adding Sn precursor.

2.3 Preparation of C-PdSn/SnO_x catalysts (10% loading)

To prepare our C-PdSn/SnO_x catalysts, we mixed a hexane dispersion of 5 mg of PdSn/SnO_x nanoparticles with 45 mg activated carbon (Vulcan XC-72R) and sonicated for 2 h. The product was then collected by centrifugation. In order to remove organic ligands on the surface of these PdSn/SnO_x nanoparticles, the catalysts were immersed in a mixture of 10 mL ethanol and 10 mL acetic acid for 10 h at 70 °C according to our previous work[26, 27]. The catalysts were washed three times with excessive ethanol and dried for 8 h in a vacuum oven at 60 °C.

2.4 Characterization

The morphology was characterized by the transmission electron microscopy (TEM, EM-420). High-resolution TEM (HRTEM), high-angle annular dark-field scanning TEM (HAADF-STEM), X-ray energy dispersive spectroscopy (X-EDS) and EDS mapping were conducted on a JEOL ARM 200CF equipped with an Oxford Instrument X-ray Energy Dispersive Spectrometer. The crystal structure was determined by the X-ray diffraction (XRD) on a Philips X' Pert PRO SUPER with Cu Kα (λ = 1.54056 Å). X-ray photoelectron spectroscopy (XPS) was performed on a PHI Versa Probe III scanning XPS microscope using a monochromatic Al K-alpha X-ray source (1486.6 eV). The element contents of the products were determined by inductively coupled plasma optical emission spectrometry (ICP-OES) on a SPECTRO GENESIS ICP spectrometer. Fourier transform infrared spectroscopy (FTIR) was performed on an Agilent Cary 630. Liquid products were analyzed by ^{1}H NMR using dimethyl sulfoxide (DMSO) as an internal standard.

2.5 Electrochemical Measurements

Electrochemical measurements were conducted on a BioLogic electrochemical workstation using a three-neck-type cell at room temperature. Pt foil was used as the counter electrode and Ag/AgCl (3.5 M KCl) was used as the reference electrode. The potential was converted to RHE according to E (vs. RHE) = E (vs. Ag/AgCl) + 0.198 V + 0.059 × pH. A glassy carbon rotating disk electrode (RDE) (PINE, 5 mm diameter, 0.19625 cm^2) was used as the substrate for catalysts. The preparation method of the working electrode can be found as follows: 5 mg of carbon-supported catalyst powder was dispersed in 1mL isopropanol with 20 μL of Nafion solution (5 wt%, Sigma-Aldrich), then the mixture was ultrasonicated for at least 30 min to generate a homogeneous ink. Next, 20 μL of the dispersion was drop-casted onto the RDE, leading to a Pd loading ~25 μg/cm^2. For comparison, the Pd loadings for C-Pd, and commercial C-Pd were ~25 μg/cm^2 as well. Finally, the as-prepared catalyst on RDE was dried at room temperature. Before the electrochemical tests, surface cleaning and activating was executed by cyclic voltammetry (CV) scanning to reach a steady-state in N_2-saturated 1 M KOH + 1 M ethanol solution for 50 cycles at room temperature with a sweep rate of 250 mV/s. CV curves were then recorded at a scan rate of 50 mV/s in N_2-saturated 1 M KOH + 1 M ethanol solution. Chronoamperometry (CA) measurements were conducted at -0.2 V vs. Ag/AgCl for 6000 s in the 1 M KOH + 1 M ethanol solution for stability evaluation. For CO stripping tests, electro-oxidation of adsorbed CO molecules was carried out in the solution of 1 M KOH. Before the test, the solution was purged with N_2 for 30min and then bubbled with CO gas (99.99%) for 15 min. The residual CO in the solution was purged by N_2 for 30 min.

2.6 *In-situ* attenuated total reflectance surface enhanced infrared absorption spectroscopy (ATR-SEIRAS) experiments.

Experiments were conducted in a one compartment PEEK spectroelectrochemical cell with the VeeMAXIII ATR accessory. A graphite rod counter electrode and a saturated Ag/AgCl reference electrode controlled by a Metrohm Autolab potentiostat were used. IR measurements were performed in a Thermo Nicolet iS50 FTIR equipped with a liquid nitrogen cooled MCT detector. All spectra were collected with a 4 cm^{-1} resolution and 32 coadded scans. Each set of 32 spectra takes approximately 12 s to complete, so at the potential sweep rate of 5 mV/s, each spectrum averages ~60 mV. A modified chemical deposition method was used to generate Au film electrodes on the reflecting plane of Si ATR crystal prisms cut to 60° incidence.[28] The Au film working electrode was cycled from -0.3 V_{RHE} to 1.2 V_{RHE} in N_2 purged 0.1 M $KHCO_3$ (Sigma Aldrich 99.7%) until the CO absorption frequency at ~2100 cm^{-1} was observed, indicating infrared surface enhancement. The activated film was rinsed with DI water and dried to remove the $KHCO_3$ electrolyte and residues from the crystal. A catalyst ink was prepared by sonicating in an ice bath a mix 1 mg of the carbon supported catalyst in 1 mL of isopropanol and 10 µL Nafion solution (5 wt%). Next, 250 µL of the desired catalyst ink was drop cast onto the film and dried. The reassembled cell was filled with 5 mL of 0.1 M KOH and N_2 purged for at least 30 minutes. All SEIRAS experiments were performed in 1 M ethanol/ 0.1 M KOH solution.

3. Results and discussion

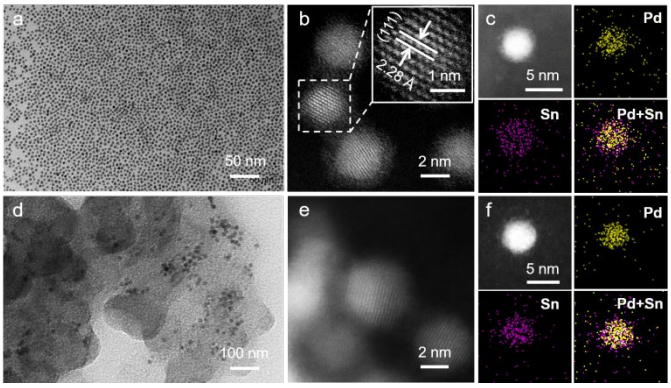

Fig. 1 Representative electron microscopy results for (a-c) as-synthesized PdSn/SnO_x nanoparticles and (d-f) the C-PdSn/SnO_x catalyst. (a) A lower magnification TEM bright-field image of PdSn/SnO_x nanoparticles. (b) A higher magnification STEM-HAADF image of PdSn/SnO_x nanoparticles, showing a structure composed of a crystalline core and amorphous shell. Inset: the HRTEM image of one single PdSn/SnO_x particle in (b). (c) The STEM-HAADF image and the corresponding X-EDS mappings of a PdSn/SnO_x particle. (d) A lower magnification TEM bright-field image of the C-PdSn/SnO_x catalyst. (e) A higher magnification STEM-HAADF image of C-PdSn/SnO_x catalyst. (f) The STEM-HAADF image and the corresponding X-EDS mappings of a PdSn/SnO_x particle on the carbon support.

The as-synthesized PdSn/SnO_x nanoparticles synthesized at the 1:1 Pd/Sn molar ratio and the final C-PdSn/SnO_x catalyst were studied using various electron microscopy techniques (Fig. 1). A representative TEM image of the PdSn/SnO_x core/shell nanoparticles is shown in Fig. 1a, demonstrating that these nanoparticles are monodispersed and highly uniform with a size of 4.5 nm ± 0.5nm. These nanoparticles appear to have a crystalline core and an amorphous shell about 0.5 nm thick (Fig. 1b). The HRTEM image shows clear lattice fringes with a lattice spacing of 2.28 Å in the core, which can be assigned to the (111) planes of PdSn alloy. The combined findings of the amorphous structure, lower Z-contrast of the shell in the STEM-HAADF image and the X-EDS mapping (Fig. 1c) suggested that the shell is SnO_x. The core is highly likely to be a Pd-rich alloy. The X-EDS mappings indicate that Sn enriches the entire nanoparticle, while Pd only distributes in the core, further confirming the PdSn/SnO_x core/shell structure. The composition was analyzed by X-EDS (Fig. S1a) and ICP-OES, and the results indicate consistently that the Pd/Sn molar ratio is about 1:1.

PdSn/SnO_x core/shell nanoparticles were then supported onto a commercial activated carbon with a high surface area. Acetic acid treatment was employed to remove organic ligands from the surface of the catalysts. FTIR results show this method can effectively remove surfactants from the surface of the PdSn/SnO_x nanoparticles (Fig. S2). The TEM image in Fig. 1d demonstrates a fairly uniform distribution of the PdSn/SnO_x core/shell nanoparticles on the carbon support after acetic acid treatment. The HRTEM image (Fig. 1e), HAADF-STEM image and the corresponding elemental mapping (Fig. 1f) demonstrated that PdSn/SnO_x nanoparticles maintained the core/shell structure after acetic acid treatment while the thickness of the SnO_x shell decreased slightly.

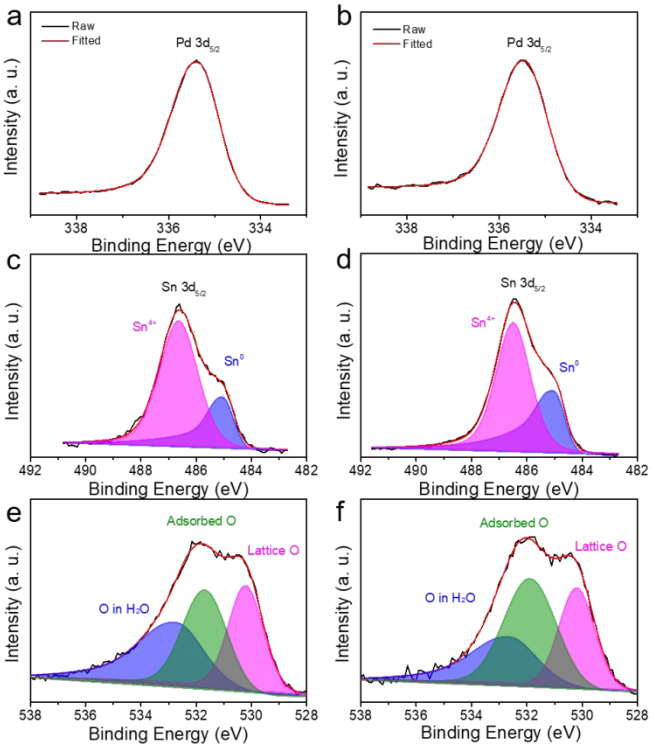

Fig. 2 High-resolution XPS spectra of (a, b) Pd 3d, (c, d) Sn 3d and (e, f) O 1s of the C-PdSn/SnO_x nanoparticles before (a, c, e) and after acetic acid treatment (b, d, f).

We also synthesized PdSn/SnO_x nanoparticles with different Pd/Sn ratios by varying the amounts of metal precursors. As shown in Fig. S3 all the PdSn/SnO_x nanoparticles are monodispersed and

relatively uniform in size. The X-ray diffraction (XRD) patterns, shown in Fig. S1b, displayed the typical face-centered cubic (*fcc*) peaks of Pd (JCPDS 87-0645). The (111) peak positions of PdSn/SnO_x core/shell nanoparticles in the XRD patterns are shifted to lower angles when compared with pure Pd due to the different lattice parameters of Pd and Sn, indicating that the Sn has been incorporated into the *fcc* Pd structures to form alloys. No SnO_x phase has been observed, confirming the amorphous nature of the SnO_x shell, consistent with our STEM observations. Moreover, in the absence of Pd precursor, SnO aggregates were obtained (Fig. S4), while Pd nanoparticles with an average size of 25 nm were produced in the absence of Sn precursor at 300 °C (Fig. S5).

The detailed structural and surface information of C-PdSn/SnO_x **nanoparticles after** acetic acid treatment was further investigated by XPS (Fig. 2 and Fig. S6). As shown in Fig. 2a, 2b, the peak at 335.4 eV can be assigned to Pd 3d5/2, up-shifted 0.5 eV with respect to Pd^0 (334.9 eV). This can be attributed to the presence of Sn that modifies the electronic structure of Pd.[14] There is no significant difference in Pd 3d5/2 spectra before and after acetic acid treatment. The **Sn 3d5/2 peak can be deconvoluted into two peaks, indicating the presence of two Sn valence states (**Fig. 2c, 2d**). The peak at the binding energy of 486.5 eV can be assigned to the oxidized Sn^{4+}, while the peak at 485.0 eV belongs to metallic Sn^0. The atom ratio of Pd/Sn on the nanoparticle surface estimated from XPS was 39:61 (**Table S1**), lower than the results from X-EDS and ICP. This observation further confirms that the PdSn nanoparticles are coated with a SnO_x shell on the surface, consistent with the** X-EDS mapping **and STEM image. The ratio of Sn^0/Sn^{4+} increased after acetic acid treatment (**Table S2**), which indicated that** SnO_x **on the surface had been partially removed after acetic acid treatment. This was further confirmed by the increased ratio of Pd/Sn after acetic acid treatment (**Table S1**). In the O 1s region (**Fig. 2e, 2f**), the fitted peaks at 530.2, 531.7 and 532.8 eV can be attributed to lattice O from** SnO_x**, adsorbed oxygen species, and O from adsorbed H_2O, respectively. The lattice O in** C-PdSn/SnO_x **after acid treatment shows lower intensity, indicating the partial removal of** SnO_x**.**

To evaluate the EOR activity of C-PdSn/SnO_x, CV was recorded in N_2-saturated solution containing 1 M KOH and 1 M ethanol at a sweep rate of 50 mV/s. C-Pd, C-SnO and commercial C-Pd (10 wt%, Johnson Matthey) reference were also tested for comparison. Before the EOR activity test, surface cleaning and activation was executed by CV scanning in N_2-saturated 1 M KOH and 1 M ethanol solution for 50 cycles at room temperature with a sweep rate of 250 mV/s. As shown in Fig. S7a, acetic acid-treated C-PdSn/SnO_x catalyst exhibited superior EOR activity (3.2 A/mg_{Pd} at 0.85 V vs. RHE) to that of as-synthesized untreated C-PdSn/SnO_x nanoparticles (1.2 A/mg_{Pd} at 0.81 V vs. RHE), which should be attributed to the clean surface and the thinner SnO_x layer on the surface after the acetic acid treatment. We also tested the EOR activities of the C-PdSn/SnO_x catalysts with different Pd/Sn ratios. The C-PdSn/SnO_x catalyst with a Pd/Sn ratio of 1:1 showed the best EOR activity (Fig. S7b). Fig. 3a displays the CV curves of C-PdSn/SnO_x C-Pd, C-SnO and commercial C-Pd catalysts at a sweep rate of 50 mV/s. C-PdSn/SnO_x catalyst exhibited much higher peak current density than that of C-Pd and commercial C-Pd catalysts, while C-SnO offered negligible EOR activity. As shown in Fig. 3b and Fig. S8, C-PdSn/SnO_x catalyst exhibited a much higher mass current density, and the peak current density of C-PdSn/SnO_x catalysts (3.2 A/mg_{Pd} at 0.85 V vs. RHE) was 3.2 and 8.2 times higher than that of the commercial C-Pd catalyst (1.0 A/mg_{Pd} at 0.83 V vs. RHE) and C-Pd catalyst (0.39 A/mg_{Pd} at 0.77 V vs. RHE), respectively. Furthermore, the onset potential for ethanol oxidation of C-PdSn/SnO_x catalysts was 80 mV lower than that of commercial C-Pd, suggesting that the EOR is more favorable on the surface of C-PdSn/SnO_x. The ratio of the peak current (I_f/I_b) between the forward scan (I_f) and the backward scan (I_b) represents the resistance to carbonaceous species poisoning. The I_f/I_b of the C-PdSn/SnO_x catalyst is 0.872, which is much higher than that of commercial C-Pd (0.634), indicating the higher tolerance to poisoning species of C-PdSn/SnO_x catalyst. Figure 3 c shows CVs of C-PdSn/SnO_x, C-Pd, and commercial C-Pd catalysts in N_2-saturated 1 M KOH solution. The electrochemical surface area (ECSA) of catalysts can be estimated from the integrated peak area of the reduction peak of PdO. The ESCA of C-PdSn/SnO_x is calculated to be 27.8 m^2/g, which is remarkably larger than those of C-Pd (8.6 m^2/g) and commercial C-Pd catalysts (13.0 m^2/g). The intrinsic activities for EOR on C-PdSn/SnO_x, C-Pd and commercial C-Pd are evaluated via normalized to ECSA (Fig. 3d). The ECSA-normalized EOR activity on C-PdSn/SnO_x is superior to those on C-Pd and commercial C-Pd catalysts (Fig. 3d). The comprehensive comparison of EOR performance of our system with other Pd-based catalysts is listed in Table S3. We found that the EOR activity of C-PdSn/SnO_x catalyst is much higher than that of most of PdSn-based catalysts, and is close to the best known EOR catalysts in alkaline media.[13, 29] **The ^{1}H NMR analyses suggested that the primary product from EOR by C-PdSn/SnO_x catalysts is acetate (Fig. S9).**

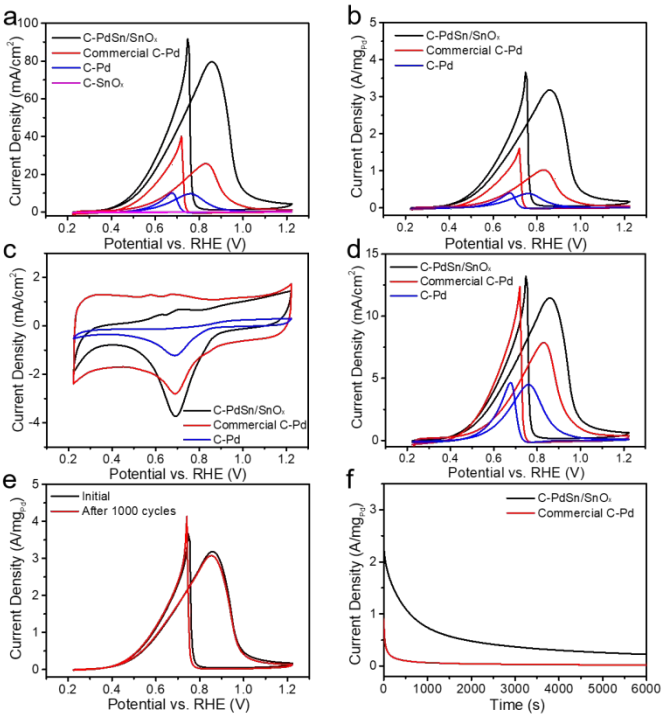

Fig. 3 (a) CV curves of ethanol oxidation for C-PdSn/SnO_x, C-Pd, C-SnO and commercial C-Pd catalysts in 1 M KOH+1 M ethanol (normalized to the electrode geometric area). (b) The mass current density (normalized to the mass of Pd) of C-PdSn/SnO_x C-Pd, and commercial C-Pd catalysts. (c) CV curves for C-PdSn/SnO_x, C-Pd, and commercial C-Pd catalysts in 1 M KOH. (d)

The ECSA-normalized EOR activity for C-PdSn/SnO_x, C-Pd, and commercial C-Pd catalysts. (e) EOR CV curves of C-PdSn/SnO_x before and after 1000 cycles of accelerated stability tests. (f) Chronoamperometric curves of C-PdSn/SnO_x and commercial C-Pd catalyst at 0.824 V vs. RHE electrode in 1 M KOH+1 M ethanol.

To further evaluate the stability of the C-PdSn/SnO_x **catalyst, accelerated degradation by repeated cycling was performed. Fig. 3e shows that the** C-PdSn/SnO_x **catalyst afforded nearly unchanged CV curves after 1000 potential cycles in 1 M KOH+1 M ethanol, only with a negligible decrease of the peak current density, while the peak current density of the commercial C-Pd decreased by about 32.4% (Fig. S10). The long-term stabilities of the** C-PdSn/SnO_x **catalyst and the commercial C-Pd for ethanol oxidation were further investigated by chronoamperometric tests in 1 M KOH+1 M ethanol at 0.824 V vs. RHE electrode, as shown in Fig. 3f. The** C-PdSn/SnO_x **catalyst is more durable than commercial C-Pd in the EOR. After the durability test, the catalysts were removed from the rotating disk electrode and characterized by TEM, which showed that the PdSn/SnO_x nanoparticles maintained the core/shell structure and fairly uniform distribution on the activated carbon support (Fig. S11a, S11b), while the severe aggregation of commercial C-Pd was observed (Fig. S11c). This can be attributed to the protecting layer of SnO_x on Pd in our PdSn/SnO_x core/shell structure.**

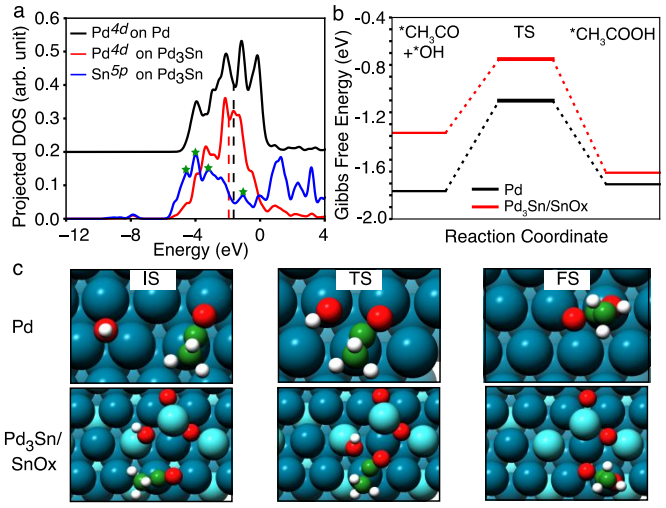

Fig. 4 (a) Projected density of states onto the Pd 4d-states of Pd(111) and Pd_3Sn(111) along with the Sn 5p-states of Pd_3Sn(111). The Pd d-band center positions are marked by vertical lines. (b) Free energy diagram of the coupling of *CH_3CO with *OH on Pd and Pd_3Sn/SnO_x model systems. (c) The structures of initial states, transition states, and final states are shown (see Fig. S13 for both top and side views of geometries).

To rationalize the activity trends observed here, we performed DFT calculations to investigate the energetics of key surface intermediates and elementary steps governing the electrocatalytic performance of surface sites toward ethanol oxidation. From previous experimental studies,[11, 30] it is generally accepted that the coupling of *CH_3CO and *OH intermediates is the rate-determining step for EOR to acetate. To represent the active site of metal nanoparticles, we chose (111)-terminated surfaces as the model system (Fig. S12) because the under-coordinated sites will likely be blocked by *OH species in relevant operating conditions and do not contribute to the measured activity. To simulate the Pd-rich core of the PdSn nanoparticles, we used the Pd_3Sn intermetallic alloy with a DFT-optimized lattice constant 4.04 Å close to the experimental value 3.95 Å,[31] (see SI for detailed information). From Fig. 4a we can see that the 4d-states of Pd and 5p-states of Sn in Pd_3Sn are strongly coupled since many peaks of two profiles are aligned (green stars). Because of the strong d-p orbital hybridization of Pd-Sn, the d-band center of the surface Pd site is lowered from -1.64 eV in Pd(111) to -1.94 eV in Pd_3Sn(111) (Fig. 4a). Moreover, the electron transfer from electron-rich Sn atoms to Pd sites will lead to a longer bond distance of the CO/carbonaceous species to the surface, thus in a weaker hybridization energy.[32] **Those two effects together result in a weakened *CH_3CO adsorption at the Pd-Pd bridge site by 0.6 eV (see Table 1 and Table S5 for geometries). The destabilization of *CH_3CO at Pd_3Sn/SnO_x leads to a facile coupling with *OH, see Fig. 4b, in which the geometries of most stable species are shown (Fig. 4c). The lowering of the d-band center is not coming from the strain effect because the lattice constant of *fcc* Pd_3Sn is actually larger than Pd, which should have led to larger Pd-Pd separations and higher d-band center, in contradiction to what we see from the DFT-calculated density of d-states. The SnO_2 clusters anchored onto the Pd_3Sn resembling amorphous SnO_x layers has no influence on the reactivity of Pd sites toward surface intermediates (Table 1), but rather provides rich Sn-Sn ensembles with favorable adsorption of *OH from the bulk electrolyte, which can be easily transferred to the Pd_3Sn surface for coupling with carbonaceous species.**

Table 1. Free formation energies of surface species on model systems relative to the gas phase CO, H_2O, and H_2. Free energy corrections of each species are shown on Table S4.

Surfaces	*CH_3CO		*CO		*OH	
	ΔG (eV)	Site	ΔG (eV)	Site	ΔG (eV)	Site
Pd	-1.78	Double top Pd	-1.90	Hol (fcc)	0.015	Hol (fcc)
Pd_3Sn	-1.18	Double top Pd	-1.53	Hol (hcp)	-0.03	Top (Sn)
Pd_3Sn/SnO_x	-1.2	Double top Pd	-1.53	Hol (hcp)	-0.07	Sn-Sn Brg

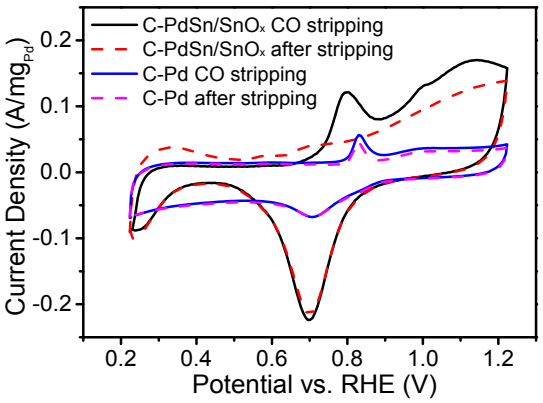

Fig. 5 CO stripping voltammograms of C-PdSn/SnO_x and commercial C-Pd catalyst in 1 M KOH at 50 mV/s.

The CO* intermediate generated from C-C cleavage could accumulate on the surface and poison the active sites.[33] Here we use CO as a probe molecule to evaluate the tolerance of C-PdSn/SnO_x to carbonaceous poisoning species. The CO stripping tests were performed in 1 M KOH at a scan rate of 50 mV/s, as shown in Fig. 5. The potential of CO oxidation on C-PdSn/SnO_x catalyst (0.80 V vs. RHE) is obviously more negative than that on commercial C-Pd (0.83 V vs. RHE), with the stripping potential of C-PdSn/SnO_x shifted negatively 30 mV as compared to potentials observed for commercial C-Pd. Furthermore, the CO oxidation peak almost disappeared after the CO stripping. In contrast, the CO adsorption peak still existed on C-Pd after stripping. The CO stripping results suggest that CO can be readily removed from the surface of C-PdSn/SnO_x, indicating an improved CO oxidation activity and excellent CO anti-poisoning during EOR.[29] This is supported by the DFT calculations (Table 1) showing that both the *CO and *CH_3CO species are significantly weakened on Pd_3Sn compared to that on Pd because of the modification of the electronic structure of Pd sites upon alloy formation. The removal of *CO by coupling with oxygen-containing species (in this case *OH) is an important aspect characterizing the stability of the electrocatalysts for EOR. Because the adsorption of *CO at Pd sites is weakened on Pd_3Sn compared to that on pure Pd, the activation barrier of the reaction CO* + OH*→COOH* is reduced (Fig. 6 and Fig. S14 for geometries), suggesting that the catalyst exhibits improved CO* poisoning resistance.

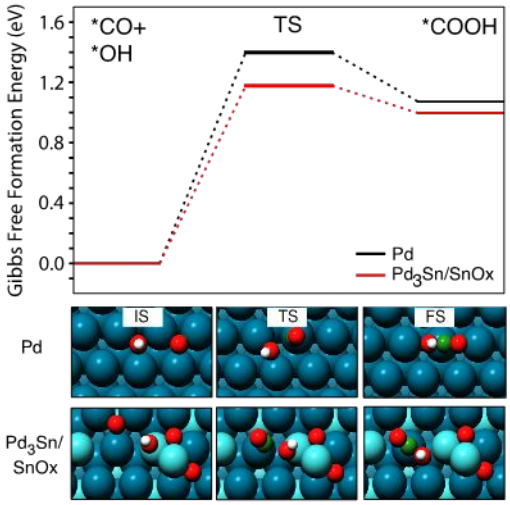

Fig. 6 Free energy diagram of the coupling of *CO with *OH on Pd and Pd_3Sn/SnO_x model systems.

Furthermore, *in-situ* ATR-SEIRAS measurement was carried out to identify the intermediates of the EOR process. Fig. 7 shows the ATR-SEIRAS spectra results collected from C-PdSn/SnO_x and commercial C-Pd during a CV cycle between -0.565 V and 1.165 V vs. RHE at 5 mV/s in 0.1 M KOH and 1 M ethanol solution (electrolyte optimized for *in-situ* measurements). As previous reports, the absorption at 1415 and 1553 cm^{-1} can be attributed to the symmetric and asymmetric stretching band of ν(OCO) in acetyl intermediate, respectively, and the absorption at 1665-1710 cm^{-1} is due to ν(CO) of adsorbed acetyl intermediate and δ(HOH) of interfacial H_2O.[25, 34] The vibrational peak at 1830 cm^{-1} of C-PdSn/SnO_x was commonly assigned to bridge-bonded CO on Pd.[35] As the potential increasing, the peak gradually disappeared due to the oxidative removal of CO (Fig. 7a), while the CO signal enhanced in the ATR-SEIRAS spectra of commercial C-Pd over the entire potential range (Fig. 7b). The absorption intensity of CO_2 (around 2340 and 2362 cm^{-1}) for C-PdSn/SnO_x increased significantly as compared to commercial C-Pd. This demonstrated that CO was more easily converted to CO_2 on the C-PdSn/SnO_x catalyst, whereas CO rapidly accumulated on commercial C-Pd during EOR electrocatalysis, which was consistent with the CO stripping experiment well. The in-situ ATR-SEIRAS results provided solid spectroscopic support for the excellent poisoning resistance and high stability of the C-PdSn/SnO_x catalyst.

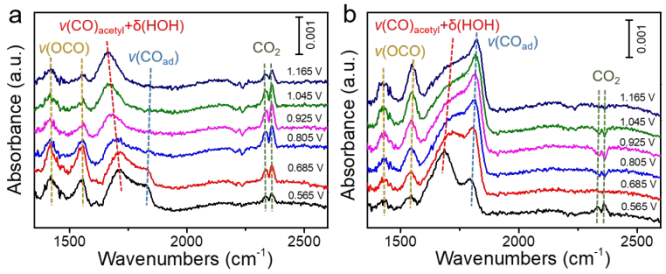

Fig. 7 ATR-SEIRAS spectra of (a) C-PdSn/SnO_x and (b) commercial C-Pd during CV cycling between 0.565 V and 1.165 V vs. RHE at 5 mV/s in 0.1 M KOH and 1 M ethanol solution.

4. Conclusions

In summary, we report the synthesis of PdSn/SnO_x core/shell nanoparticles as a high-performance catalyst for the EOR. After supported on activated carbon, this core/shell structure demonstrated substantially enhanced EOR activity and durability compared with that of commercial C-Pd catalysts. DFT calculations reveal that the enhanced catalytic performance originates from the weakening of carbonaceous species, e.g., *CH_3CO and *CO, facilitating their coupling with *OH for the formation of acetate and alleviating the surface poisoning. The existence of amorphous SnO_x layers provides a shuttling path for the formation of more stable *OH species from the bulk electrolyte. The strategy of employing the synergy at PdSn and SnO_x interface to simultaneously promote electrocatalytic activity and durability of EOR is broadly applicable and can be extended to other nanoparticle electrocatalyst systems for energy conversion and other important reactions.

Conflicts of interest

There are no conflicts to declare.

Acknowledgements

Q.G. and H.Z. acknowledges the start-up fund from Virginia Polytechnic Institute and State University. Q.H. acknowledges the support by the National Research Foundation (NRF) Singapore, under its NRF Fellowship (NRF-NRFF11-2019-0002). T.M. and H.X. acknowledge financial support from the NSF CAREER program (CBET-1845531). The computational resource used in this work is provided by the advanced research computing at Virginia Polytechnic Institute and State University.

Notes and references

1. Z. Luo, J. Lu, C. Flox, R. Nafria, A. Genç, J. Arbiol, J. Llorca, M. Ibáñez, J. R. Morante and A. Cabot, *J. Mater. Chem. A*, 2016, **4**, 16706-16713.
2. Y.-J. Wang, J. Qiao, R. Baker and J. Zhang, *Chem. Soc. Rev.*, 2013, **42**, 5768-5787.
3. L. An and T. S. Zhao, *Energy Environ. Sci.*, 2011, **4**, 2213-2217.
4. J. Mao, W. Chen, D. He, J. Wan, J. Pei, J. Dong, Y. Wang, P. An, Z. Jin, W. Xing, H. Tang, Z. Zhuang, X. Liang, Y. Huang, G. Zhou, L. Wang, D. Wang and Y. Li, *Sci. Adv.*, 2017, **3**, e1603068.
5. L. An, T. S. Zhao and Y. S. Li, *Renew. Sust. Energ. Rev.*, 2015, **50**, 1462-1468.
6. H. Wu, H. Li, Y. Zhai, X. Xu and Y. Jin, *Adv. Mater.*, 2012, **24**, 1594-1597.
7. E. Antolini, *J. Power Sources*, 2007, **170**, 1-12.
8. P. Wang, S. Yin, Y. Wen, Z. Tian, N. Wang, J. Key, S. Wang and P. K. Shen, *ACS Appl. Mater. Interfaces*, 2017, **9**, 9584-9591.
9. G. Jiang, H. Zhu, X. Zhang, B. Shen, L. Wu, S. Zhang, G. Lu, Z. Wu and S. Sun, *ACS Nano*, 2015, **9**, 11014-11022.
10. M. Iqbal, Y. V. Kaneti, J. Kim, B. Yuliarto, Y.-M. Kang, Y. Bando, Y. Sugahara and Y. Yamauchi, *Small*, 2019, **15**, 1804378.
11. C. Bianchini and P. K. Shen, *Chem. Rev.*, 2009, **109**, 4183-4206.
12. Q. Gao, Y. M. Ju, D. An, M. R. Gao, C. H. Cui, J. W. Liu, H. P. Cong and S. H. Yu, *ChemSusChem*, 2013, **6**, 1878-1882.
13. K. Jiang, P. Wang, S. Guo, X. Zhang, X. Shen, G. Lu, D. Su and X. Huang, *Angew. Chem., Int. Ed.*, 2016, **55**, 9030-9035.
14. L.-X. Ding, A.-L. Wang, Y.-N. Ou, Q. Li, R. Guo, W.-X. Zhao, Y.-X. Tong and G.-R. Li, *Sc.i Rep.*, 2013, **3**, 1181.
15. X. Yu, Z. Luo, T. Zhang, P. Tang, J. Li, X. Wang, J. Llorca, J. Arbiol, J. Liu and A. Cabot, *Chem. Mater.*, 2020, **32**, 2044-2052.
16. B. Cai, D. Wen, W. Liu, A. K. Herrmann, A. Benad and A. Eychmuller, *Angew. Chem., Int. Ed.*, 2015, **54**, 13101-13105.
17. W. Du, K. E. Mackenzie, D. F. Milano, N. A. Deskins, D. Su and X. Teng, *Acs Catal.*, 2012, **2**, 287-297.
18. Y. Feng, Q. Shao, B. Huang, J. Zhang and X. Huang, *Natl. Sci. Rev.*, 2018, **5**, 895-906.
19. H. Zhu, A. Sigdel, S. Zhang, D. Su, Z. Xi, Q. Li and S. Sun, *Angew. Chem., Int. Ed.*, 2014, **53**, 12508-12512.
20. K. Yu, Z. Wu, Q. Zhao, B. Li and Y. Xie, *J. Phys. Chem. C*, 2008, **112**, 2244-2247.
21. Z. Zhuang, W. Sheng and Y. Yan, *Adv. Mater.*, 2014, **26**, 3950-3955.
22. R. Wang, Z. Liu, Y. Ma, H. Wang, V. Linkov and S. Ji, *Int. J. Hydrog. Energy*, 2013, **38**, 13604-13610.
23. A. Kowal, M. Li, M. Shao, K. Sasaki, M. B. Vukmirovic, J. Zhang, N. S. Marinkovic, P. Liu, A. I. Frenkel and R. R. Adzic, *Nat. Mater.*, 2009, **8**, 325-330.
24. L. Jiang, G. Sun, S. Sun, J. Liu, S. Tang, H. Li, B. Zhou and Q. Xin, *Electrochim. Acta*, 2005, **50**, 5384-5389.
25. Y.-Y. Yang, J. Ren, Q.-X. Li, Z.-Y. Zhou, S.-G. Sun and W.-B. Cai, *Acs Catal.*, 2014, **4**, 798-803.
26. Z. Zhang, M. Chi, G. M. Veith, P. Zhang, D. A. Lutterman, J. Rosenthal, S. H. Overbury, S. Dai and H. Zhu, *Acs Catal.*, 2016, **6**, 6255-6264.
27. H. Zhu, S. Zhang, S. Guo, D. Su and S. Sun, *J. Am. Chem. Soc.*, 2013, **135**, 7130-7133.
28. M. Dunwell, Q. Lu, J. M. Heyes, J. Rosen, J. G. Chen, Y. Yan, F. Jiao and B. Xu, *J. Am. Chem. Soc.*, 2017, **139**, 3774-3783.
29. L. Chen, L. Lu, H. Zhu, Y. Chen, Y. Huang, Y. Li and L. Wang, *Nat. Commun.*, 2017, **8**, 14136.
30. Z. Liang, T. Zhao, J. B. Xu and L. Zhu, *Electrochim. Acta*, 2009, **54**, 2203-2208.
31. Z. Liu and X. Zhang, *Electrochem. Commun.*, 2009, **11**, 1667-1670.
32. H. Xin and S. Linic, *J. Chem. Phys.*, 2010, **132**, 221101.
33. S. Shen, Y. Guo, L. Luo, F. Li, L. Li, G. Wei, J. Yin, C. Ke and J. Zhang, *J. Phys. Chem. C*, 2018, **122**, 1604-1611.
34. N.-F. Yu, N. Tian, Z.-Y. Zhou, T. Sheng, W.-F. Lin, J.-Y. Ye, S. Liu, H.-B. Ma and S.-G. Sun, *Acs Catal.*, 2019, **9**, 3144-3152.
35. W. Huang, X.-Y. Ma, H. Wang, R. Feng, J. Zhou, P. N. Duchesne, P. Zhang, F. Chen, N. Han, F. Zhao, J. Zhou, W.-B. Cai and Y. Li, *Adv. Mater.*, 2017, **29**, 1703057.